

# Stellar ( $n, \gamma$ ) cross sections of $^{23}\text{Na}$

E. Uberseder

*Karlsruhe Institute of Technology (KIT), Campus North,  
Institute of Nuclear Physics, PO Box 3640, Karlsruhe, Germany and  
University of Notre Dame, Department of Physics, Notre Dame, IN 46556, USA\**

M. Heil<sup>†</sup>

*GSI Darmstadt, Planckstr. 1, 64291 Darmstadt, Germany*

F. Käppeler

*Karlsruhe Institute of Technology (KIT), Campus North,  
Institute of Nuclear Physics, PO Box 3640, Karlsruhe, Germany*

C. Lederer

*School of Physics and Astronomy, University of Edinburgh, UK*

A. Mengoni

*ENEA, 40100 Bologna, Italy*

S. Bisterzo

*INAF, Astrophysical Observatory of Turin, 10025 Pino Torinese, Italy and  
INFN, Sezione di Torino, Via P. Giuria 1, 10125 Torino, Italy*

M. Pignatari

*E.A. Milne Centre for Astrophysics, Dept of Physics & Mathematics,  
University of Hull, HU6 7RX, United Kingdom and  
NuGrid collaboration, <http://www.nugridstars.org>*

M. Wiescher

*University of Notre Dame, Department of Physics, Notre Dame, IN 46556, USA\**

(Dated: February 7, 2017)

The cross section of the  $^{23}\text{Na}(n, \gamma)^{24}\text{Na}$  reaction has been measured via the activation method at the Karlsruhe 3.7 MV Van de Graaff accelerator. NaCl samples were exposed to quasistellar neutron spectra at  $kT = 5.1$  and 25 keV produced via the  $^{18}\text{O}(p, n)^{18}\text{F}$  and  $^7\text{Li}(p, n)^7\text{Be}$  reactions, respectively. The derived capture cross sections  $\langle \sigma \rangle_{kT=5\text{keV}} = 9.1 \pm 0.3$  mb and  $\langle \sigma \rangle_{kT=25\text{keV}} = 2.03 \pm 0.05$  mb are significantly lower than reported in literature. These results were used to substantially revise the radiative width of the first  $^{23}\text{Na}$  resonance and to establish an improved set of Maxwellian average cross sections. The implications of the lower capture cross section for current models of  $s$ -process nucleosynthesis are discussed.

PACS numbers: 25.40.Lw, 26.20.Kn, 27.30.+t, 28.41.Fr, 97.10.Cv

Keywords: neutron activation, stellar ( $n, \gamma$ ) cross section,  $s$  process

## I. INTRODUCTION

Sodium represents a neutron poison for the slow neutron capture ( $s$ ) process, particularly in massive stars with more than about eight solar masses ( $>8 M_{\odot}$ ) [1]. The  $s$  process in massive stars is particularly efficient in producing species in the mass range  $60 < A < 90$ , forming the weak  $s$ -process component in the inventory of the solar abundances. In addition to its importance for the neutron balance in massive stars, the ( $n, \gamma$ ) cross sec-

tion of  $^{23}\text{Na}$  is also needed to follow the production of sodium in low and intermediate mass asymptotic giant branch (AGB) stars. In these stars, the *main s* process contributes most of the  $s$  abundances in the solar system from Zr to Pb, and the *strong s*-process adds to the Pb/Bi abundances at the termination point of the  $s$ -process reaction path [2, 3].

The weak  $s$  process in massive stars begins at the end of convective core He-burning ( $T_8 > 2.5$ ), where  $^{22}\text{Ne}(\alpha, n)^{25}\text{Mg}$  operates as the principal neutron source. During that period, sodium is only marginally produced by neutron captures on  $^{22}\text{Ne}$ . During the subsequent convective C-shell burning, sodium is efficiently made via the  $^{12}\text{C}(^{12}\text{C}, p)^{23}\text{Na}$  channel although most of the protons (and sodium) are consumed by  $^{23}\text{Na}(p, \alpha)^{20}\text{Ne}$  reactions

\*present address: Texas A&M University, TX 77843, USA

<sup>†</sup>corresponding author: m.heil@gsi.de

[4]. Nevertheless, the C-burning layers of massive stars ejected in the subsequent supernova (SN) are one of the major sources of sodium in the Galaxy [5, 6], together with stellar winds from AGB stars (e.g. [7]). In the convective C-burning shell, neutrons are mainly released via  $^{22}\text{Ne}(\alpha, n)^{25}\text{Mg}$  reactions as  $^{22}\text{Ne}$  is present in the ashes of the convective He-burning core and  $\alpha$  particles are liberated in  $^{12}\text{C}(^{12}\text{C}, \alpha)^{20}\text{Ne}$  reactions (e.g. [8]).

In the weak  $s$  process most of the neutrons are captured by abundant light isotopes, which act as neutron poisons, and only a small fraction is available for captures on iron seed nuclei to feed heavy isotope nucleosynthesis. At solar metallicity, more than 70% of the available neutrons are captured by neutron poisons in the He-burning core, and more than 90% in the C-burning shell. For this reason, it is extremely important to quantify the neutron capture rates of light isotopes such as sodium to evaluate the impact of neutron poisons in the weak  $s$  process.

Another relevant source for the production of sodium are thermally pulsing low-mass (e.g., [9–11]) and massive AGB stars [12], where the  $s$  process is related to the He shell burning stage of evolution. In a first episode, neutrons are produced by  $^{13}\text{C}(\alpha, n)^{16}\text{O}$  reactions during the interpulse phase between He shell flashes at temperatures of  $T_8=0.9$  ( $kT=8$  keV) [13]. The mixing of protons with the top layer of the He shell, required to provide the necessary  $^{13}\text{C}$  for neutron production, has the additional effect of activating the NeNa cycle in the partial mixing zone [10], which then continues in the H-burning shell throughout the interpulse phase [9]. A second, weaker neutron exposure takes place during the He shell flash at higher temperatures of  $T_8=2.6$  ( $kT=23$  keV) when the  $^{22}\text{Ne}(\alpha, n)^{25}\text{Mg}$  source is marginally activated. As the He flash engulfs the ashes of the H burning shell, further  $^{23}\text{Na}$  might be produced by neutron captures on the abundant  $^{22}\text{Ne}$  during this second phase of  $s$ -processing in thermally pulsing AGB stars. Recent studies by Cristallo *et al.* [14] and Bisterzo *et al.* [15] confirm that neutron capture production of primary sodium is particularly efficient in low-mass AGB stars of low metallicity.

Intermediate-mass AGB models experience hot hydrogen burning (HBB), which modifies the Na abundance on the stellar surface depending on the attained temperature and on the interplay with the efficiency for third dredge up [16, 17].

Despite of its relevance for nuclear astrophysics, the Maxwellian averaged neutron capture cross section (MACS) of  $^{23}\text{Na}$  is rather uncertain [18]. In this work, we present new experimental data for  $^{23}\text{Na}$  measured in quasi-stellar neutron spectra at thermal energies of  $kT = 5.1$  and 25 keV. Appropriate spectra have been obtained via the  $^{18}\text{O}(p, n)^{18}\text{F}$  and  $^7\text{Li}(p, n)^7\text{Be}$  reactions to simulate stellar temperature conditions relevant to  $s$ -process nucleosynthesis. The experimental details and results of the activation measurements are given in Secs. II and III. In Sec. IV, MACS values are derived for the full range of  $s$ -process temperatures on the basis of the

present results. The implications of these data for the  $s$ -process abundances are discussed for massive stars as well as for AGB stars.

## II. EXPERIMENT

Similar to many light nuclei, the  $^{23}\text{Na}(n, \gamma)^{24}\text{Na}$  cross section is difficult to study experimentally given the high ratio of scattering to capture cross sections. In such cases, neutrons scattered on the sample and subsequently captured in or near the detector can induce a large background when measuring prompt capture gammas with the time of flight (TOF) technique [19]. These difficulties can be avoided with the activation method, because the induced activity of the product nucleus is counted only after the irradiation in a low background environment. Therefore, the activation technique is well suited to measure  $(n, \gamma)$  cross sections of light nuclei with greater precision than reported previously from TOF measurements.

The experiment was carried out by a series of repeated irradiations with a set of different samples and by variation of the relevant activation parameters. In this way, corrections concerning the dimensions of the samples, self absorption, and the decay during irradiations could be constrained and the determination of systematic uncertainties improved.

### A. Samples

The samples for the individual runs were prepared from NaCl (99.99% pure) pressed into cylindrical pellets 6, 8, 10, and 15 mm in diameter with varying thicknesses. As NaCl is hygroscopic, care was taken to be sure that the water content of the material gave a negligible contribution to the mass. This was verified by heating a quantity of the NaCl at 250 °C for two hours, showing that the sample mass before and after heating differed by less than 0.01%.

The sodium cross section was measured relative to that of gold, which is commonly used as a reference in activation measurements. Gold foils 0.03 mm in thickness were cut to the proper diameters and fixed to the front and back of the samples during irradiation. The sample masses, as well as those of the respective gold foils, are given in Table I.

### B. Neutron irradiations

All neutron irradiations were performed at the Karlsruhe 3.7 MV Van de Graaff accelerator. The  $^7\text{Li}(p, n)^7\text{Be}$  reaction was utilized to obtain a thermal neutron spectrum at  $kT = 25$  keV [20–23]. The target was produced by evaporation of 30  $\mu\text{m}$  of lithium onto a water-cooled copper backing and was transported to

TABLE I: Sample characteristics

Sample	Diameter (mm)	Sample mass <sup>a</sup> (mg)		Mass of Au foils (mg)	
		NaCl	Na	upstream	downstream
Na-1	6	54.06	21.27	16.49	16.40
Na-2	8	82.67	32.52	27.92	28.47
Na-3	10	88.28	34.73	45.36	43.54
Na-4	10	232.4	91.42	43.92	44.07
Na-5	10	307.6	121.0	43.80	42.98
Na-6	15	500.1	196.7	97.76	98.47

<sup>a</sup>Uncertainties always less than 0.05 mg.

the beamline in an argon atmosphere to prevent oxidation. The required proton beam energy of  $E_p = 1912$  keV was adjusted 31 keV above the reaction threshold at 1881 keV. Due to the kinematics of the  ${}^7\text{Li}(p, n){}^7\text{Be}$  reaction, neutrons are emitted in a forward cone with an opening angle of  $120^\circ$ . As the Maxwellian neutron distribution is obtained by angular integration over the entire forward cone, care was taken to be sure that the samples of varying diameters always extended through the full solid angle.

Correspondingly, the  ${}^{18}\text{O}(p, n){}^{18}\text{F}$  reaction has been used to reproduce a thermal neutron distribution at  $kT = 5.1$  keV [24] as shown in Fig. 1. The target consisted of a 0.2-mm-thick tantalum disk with an oxide layer about  $2 \mu\text{m}$  in thickness, which was produced by electrolysis of water with 95% enrichment in  ${}^{18}\text{O}$ . The tantalum disk was glued onto a 1-mm-thick water-cooled copper backing. The glue was suited for vacuum applications and was particularly selected to obtain good heat contact with the copper backing. Also in this case, the proper proton energy of  $E_p = 2582$  keV was calibrated against the nearby reaction threshold at  $E_p = 2574$  keV, and care was taken that the sample extended through the full forward cone of the neutron beam.

The neutron flux during the runs at  $kT = 25$  keV was recorded by a lithium glass monitor, mounted on the beam axis at a distance of 831 mm from the target. Due to the much lower neutron yield for the irradiations at  $kT = 5.1$  keV, the lithium glass monitor was replaced by a more sensitive ZnS detector. The irradiation times,  $t_b$ , for each run are listed in Table II. The proton beam current was typically  $100 \mu\text{A}$  in all irradiations.

### C. Measurement of induced activity

A high purity (HP) Ge detector of  $39 \text{ cm}^3$  was utilized to measure the induced activities in the sodium samples and gold foils following the  $kT = 25$  keV runs. The efficiency of the detector as a function of energy was determined with several calibrated sources to an accuracy of 1.5%. A relatively large source-detector distance of 76 mm reduced the effect of coincidence summing. To reduce natural backgrounds, the detector was shielded with

TABLE II: Irradiation, transfer, and measuring times

Sample	$t_b$ (h)	$t_w$ (min)	$t_m$ (h)
Na-1	16.3	34.7	8.56
Na-2	21.0	26.8	10.0
Na-3	24.7	33.0	5.00
Na-4	13.8	7.20	72.7
Na-5	17.6	3.00	21.6
Na-6	19.6	4.00	22.2

50 mm lead and 5 mm copper. The measuring times,  $t_m$ , as well as the waiting times between irradiation and the  $\gamma$  counting,  $t_w$ , are listed in Table II.

Due to the much lower neutron flux reached during the irradiations with the  ${}^{18}\text{O}$  target, the weak induced activities had to be determined with a more sensitive setup consisting of two HPGe clover detectors with the sample centered between the detectors in very close geometry as described in detail by Dababneh *et al.* [25]. Again, the photo-peak efficiency was determined using several calibrated sources. In this case, the small source-detector distance required the application of corrections for summing effects and for the sample size. These, along with self absorption corrections, were determined by Monte Carlo simulations with the GEANT4 toolkit [26] using a precise modeling of the apparatus. The 1369 keV  $\gamma$ -ray from the  ${}^{24}\text{Na}$  decay was chosen for the analysis and appeared prominently above background. Figure 2 shows the 1369 keV line from the 6 mm NaCl sample after activation in the  $kT = 25$  keV spectrum. It should be noted that a short-lived (20 ms) isomeric state exists in  ${}^{24}\text{Na}$ , which has a very small probability to decay directly to  ${}^{24}\text{Mg}$  without producing a 1369 keV  $\gamma$ -ray. Endt *et al.* [27] quote this probability to be 0.05%, thus it was considered to have a negligible effect on the present measurement.

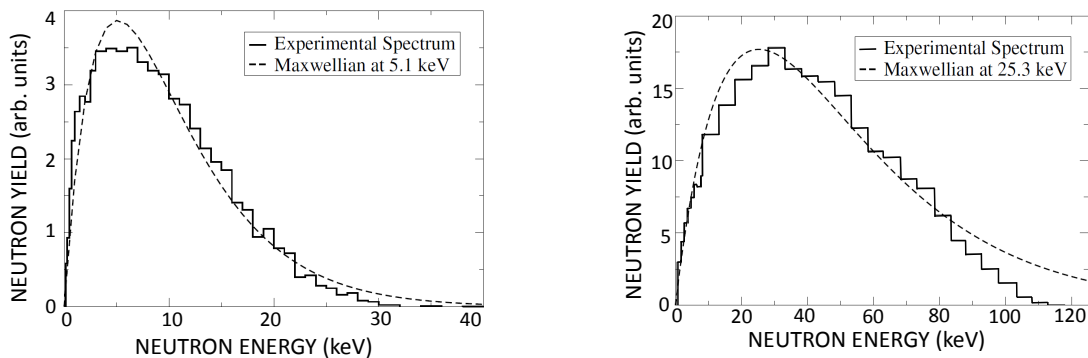


FIG. 1: Experimental neutron distributions at  $kT = 5.1$  keV (left) and 25 keV (right) compared to the respective Maxwell-Boltzmann spectra.

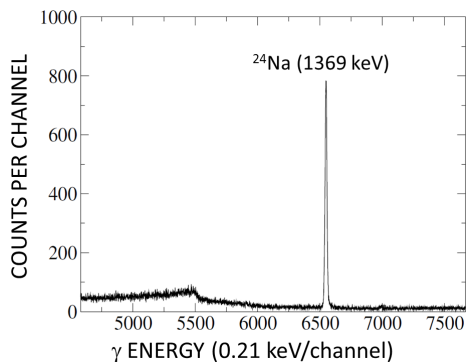


FIG. 2:  $\gamma$  Spectrum for sample Na-1 after irradiation at  $kT = 25$  keV.

### III. ANALYSIS AND RESULTS

The process to extract a cross section from the activation data follows the approach of Ref. [20]. The number of activated nuclei is defined as

$$A = \Phi_{tot} N \sigma f_b, \quad (1)$$

where  $\Phi_{tot} = \int \Phi(t) dt$  represents the time integrated neutron flux,  $N$  is the number of sample atoms, and  $\sigma$  the cross section in  $\text{cm}^2$ . The correction

$$f_b = \frac{\int_0^{t_b} \Phi(t) e^{-\lambda(t_b-t)} dt}{\int_0^{t_b} \Phi(t) dt}.$$

for decays of the produced nuclei during the irradiation phase was determined from the time-dependent yield recorded by the before mentioned lithium glass or zinc sulfide monitors, which was recorded as counts per 60 s intervals. The time integrated neutron flux was determined from the activity of the gold foils. The counts registered in the HPGe detectors are expressed as a function of the induced activity,

$$C = AK_\gamma \epsilon_\gamma I_\gamma e^{-\lambda t_w} (1 - e^{-\lambda t_m}). \quad (2)$$

where  $K_\gamma$  is the total correction factor for self absorption, summing, and sample size effects,  $\epsilon_\gamma$  the peak efficiency of the HPGe detector, and  $I_\gamma$  the absolute gamma intensity per decay of the activated nuclei. These quantities are given in Table III.

The adopted half-lives of  $^{24}\text{Na}$  and  $^{198}\text{Au}$  were  $14.9590 \pm 0.0012$  h [27] and  $2.69517 \pm 0.00021$  d [28], respectively.

The  $^{197}\text{Au}$  cross sections that are needed for the determination of  $\Phi_{tot}$  were determined in the following way: The cross sections averaged over the experimental spectra as well as the respective Maxwellian average spectra at  $kT = 5$  and 25 keV were calculated using the evaluated gold cross section from the JEFF-3.2 data library [29]. These results were then corrected for the 1.1 and 1.2% differences found with respect to the recommended MACS values in the KADoNiS-1.0 compilation [30]. The adopted spectrum-averaged gold cross sections are  $\sigma_{exp} = 637 \pm 13$  mb for  $kT = 25$  keV and  $\sigma_{exp} = 1922 \pm 70$  mb for  $kT = 5.1$  keV.

The experimental results of the activations are summarized in Table IV. Statistical and systematic errors are quoted separately. The statistical errors arise from the counting of the induced activities and from the corrections applied as a result of the Monte Carlo simulations. Sources of systematic error are listed in Table V.

### IV. ASTROPHYSICAL IMPLICATIONS

#### A. Maxwellian Averaged Cross Sections

As neutrons are quickly thermalized in a stellar environment, the stellar spectra can be described by a Maxwell-Boltzmann distribution. The MACS of an isotope exposed to such a neutron distribution is

$$\langle \sigma \rangle_{kT} = \frac{\langle \sigma v \rangle}{v_T} = \frac{2}{\sqrt{\pi}} \frac{\int_0^\infty \sigma(E_n) E_n e^{-E_n/kT} dE_n}{\int_0^\infty E_n e^{-E_n/kT} dE_n} \quad (3)$$

[31]. While the experimental spectra closely reproduce Maxwellian distributions, the small differences from a

TABLE III: Decay characteristics and absolute  $\gamma$  efficiencies

Nucleus	$t_{1/2}$	$E_\gamma$ (keV)	$I_\gamma$ (%)	$\epsilon_\gamma$ (%)	
				$kT = 5.1$ keV	25 keV
$^{24}\text{Na}$	$14.9590 \pm 0.0012$ h	1368.63	$100.00 \pm 0.0^a$	$6.94 \pm 0.10$	$0.048 \pm 0.001$
$^{198}\text{Au}$	$2.69517 \pm 0.00021$ d	411.80	$95.58 \pm 0.12^b$	$20.6 \pm 0.3$	$0.224 \pm 0.01$

<sup>a</sup>Ref. [27]<sup>b</sup>Ref. [28]TABLE IV: Measured  $(n, \gamma)$  cross sections of  $^{23}\text{Na}$  (in mb)

$kT = 5.1$ keV		$kT = 25$ keV	
Sample	$\sigma_{exp} \pm \text{syst} \pm \text{stat}$	Sample	$\sigma_{exp} \pm \text{syst} \pm \text{stat}$
Na-4	$9.03 \pm 0.28 \pm 0.26$	Na-1	$2.05 \pm 0.06 \pm 0.02$
Na-5	$8.94 \pm 0.27 \pm 0.14$	Na-2	$2.02 \pm 0.05 \pm 0.01$
Na-6	$9.33 \pm 0.29 \pm 0.14$	Na-3	$2.03 \pm 0.05 \pm 0.02$
Average	$9.10 \pm 0.28 \pm 0.11$		$2.03 \pm 0.05 \pm 0.01$

TABLE V: Systematic uncertainties (in %) of the measured  $(n, \gamma)$  cross section of  $^{23}\text{Na}$ 

Source	$kT = 5.1$ keV		$kT = 25$ keV	
	Au	Na	Au	Na
Time and decay factors	0.5	0.5	0.6	0.5
Au cross section	2.0	N/A	1.4	N/A
Sample atoms	0.1	<0.1	0.2	0.1
Self absorption	N/A	N/A	<0.1	<0.1
Detector peak efficiency	1.5	1.5	1.5	1.5
Intensity of $\gamma$ -decay branch	0.1	<0.1	0.1	<0.1
Neutron flux $\Phi_T$	N/A	3.8	N/A	2.1
Total		3.1		2.7

true MACS must still be accounted for. This is done by folding the experimental neutron distribution with the capture cross section provided by a database to yield a normalization, which is then applied to produce a true MACS calculated from the evaluated energy-dependent cross section. This method supplies a sufficiently accurate approximation for the MACS in the local energy region of the measurement, but is prone to increasing uncertainty in extrapolation to cover the full thermal energy region of stellar  $s$ -process scenarios from  $kT \approx 8$ -90 keV.

The MACS values for  $^{23}\text{Na}$  at  $kT = 5$  and 25 keV are influenced by a broad s-wave resonance at 2.8 keV, a smaller p-wave resonance at 35 keV, and a broad p-wave resonance at 53 keV. For the present analysis, the  $(n, \gamma)$  cross section was modeled by means of the R-matrix code SAMMY [32], starting with resonance energies and widths of all resonances up to 500 keV listed in the ENDF/B-VII.1 data library [33].

In addition to the resonance terms, an s-wave direct radiative capture (DRC) component in the  $^{23}\text{Na}$  cross section was included by a set of optical model DRC cal-

culations [34], using the spectroscopic factors of Ref. [35]. The contribution of the DRC component to the measured spectrum-averaged cross section is rather small but it is important for obtaining a consistent reproduction of the thermal cross section data. In fact, a DRC component of 170 mb at thermal energy with a  $1/v$  energy dependence is required to reproduce the thermal capture cross section as well as to match the resonance integral.

The resulting energy-dependent cross section was then folded with the experimental neutron spectra to produce cross sections that could be directly compared with the activation results. It turned out that it was sufficient to reduce only the radiation width of the resonance at 2.8 keV by 35% in order to reproduce the measured cross sections, while leaving the widths of the other resonances fixed. As shown in Table VI, the measured cross sections and the corresponding values obtained with this best-fit solution agreed to better than 2%. Without any further changes, the thermal cross section [36] and also the resonance integral [37] could be reproduced by this best fit as well.

The uncertainty of the radiative width for the 2.8 keV resonance was determined by variation of the SAMMY fit to match the uncertainty of the measured cross section values, yielding  $\Gamma_\gamma = 245 \pm 8$  meV. This corresponds to an improvement by a factor of three compared to the (optimistic) 10% uncertainty quoted in the early work by Friesenhahn *et al.* [38].

With the corrected strength of the 2.8-keV resonance, the best-fit solution for the capture cross section has been used to establish the updated set of MACS values for  $^{23}\text{Na}$ . The effect of the reduced and more accurate  $\Gamma_\gamma$  value of the 2.8 keV resonance is illustrated in Table VII by the comparison of these results with the data set in the KADoNiS v0.3 compilation [39] and with the evaluated cross section from the ENDF/B-VII.1 data library [33], which shows a significant reduction in the MACS values especially at thermal energies below 30 keV. The effect of the revised radiative width of the 2.8 keV resonance is most pronounced for the MACS values at  $kT = 5$  and 10 keV, which are lower by  $\sim 30$  and 20%, respectively, whereas it reduces the 25-keV MACS only by  $\sim 4\%$ .

The uncertainties quoted for thermal energies of  $kT = 5$  and 25 keV could directly be taken from the experimental values, but slightly larger uncertainties have to be considered otherwise to account for the different weights of the involved resonances, which are changing with thermal energy. Below 30 keV this additional uncertainty is

TABLE VI: Measured cross sections and calculated spectrum-averaged values

Neutron spectrum (keV)	Spectrum-averaged cross sections (mb)		
	ENDF/B-VII.1	Experimental value	SAMMY best-fit
25.3 $10^{-6}$ (thermal)	528	$541 \pm 3^a$	542
Resonance integral	312.3	$311 \pm 10^b$	300
5.1 (q-MB)	12.5	$9.10 \pm 0.30$	9.07
25 (q-MB)	2.16	$2.03 \pm 0.05$	2.00

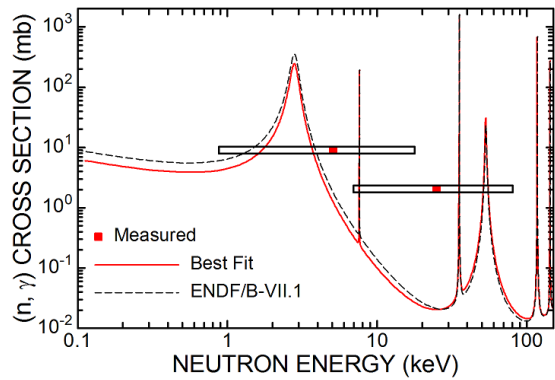
<sup>a</sup>Ref. [36]<sup>b</sup>Ref. [37]

FIG. 3: The measured spectrum averaged cross sections (full squares) and the best-fit solution obtained with the R-matrix code SAMMY [32], which is fully consistent with the data points (solid line). The FWHM of the neutron spectra are indicated by open boxes. The comparison with the ENDF/B-VII.1 evaluation [33] (dashed line) shows that it was sufficient to correct only the first resonance at 2.8 keV.

less than 3%, because only the first resonance had to be corrected to reproduce the 25-keV cross section. Towards higher values of  $kT$ , where an increasing number of resonances is contributing, this uncertainty is expected to grow and may reach 10% at  $kT = 100$  keV.

The correction of these MACS values for the effect of thermally excited nuclear states, the so-called stellar enhancement factor, is negligible over the entire range of  $s$ -process temperatures [40].

## B. Massive stars

The  $s$  process in massive stars is known to produce most of the  $s$  isotopes in the solar system between Fe and Sr (see [3] and references therein). In the convective He core, the neutron exposure starts to increase only in the last phase, close to He exhaustion, when the temperature is high enough to efficiently burn  $^{22}\text{Ne}$  via  $^{22}\text{Ne}(\alpha, n)^{25}\text{Mg}$ . The  $^{22}\text{Ne}$  available at the end of the He core phase is given by the initial abundance of the CNO nuclei. As CNO elements are converted to  $^{14}\text{N}$  in the previous H-burning core,  $^{14}\text{N}$  is converted to  $^{18}\text{O}$  via the reaction channel  $^{14}\text{N}(\alpha, \gamma)^{18}\text{F}(\beta^+)^{18}\text{O}$  at the beginning

of the He-burning core and then to  $^{22}\text{Ne}$  by  $\alpha$ -captures when the temperature exceeds  $T_8 = 2.5$ . At the point of He exhaustion the most abundant isotopes are  $^{16}\text{O}$ ,  $^{12}\text{C}$ ,  $^{20,22}\text{Ne}$  and  $^{25,26}\text{Mg}$ , where the final  $^{12}\text{C}$  and  $^{16}\text{O}$  abundances are defined by the  $^{12}\text{C}(\alpha, \gamma)^{16}\text{O}$  reaction. In He core conditions,  $^{23}\text{Na}$  is produced by the neutron capture channel  $^{22}\text{Ne}(n, \gamma)^{23}\text{Ne}(\beta^-)^{23}\text{Na}$ , and it is depleted via  $^{23}\text{Na}(n, \gamma)^{24}\text{Na}$ .

In the convective C shell the neutron exposure starts to increase during C ignition at the bottom of the shell, where neutrons are mainly produced again by the  $^{22}\text{Ne}(\alpha, n)^{25}\text{Mg}$  reaction. Typical temperatures at the bottom of the C shell are  $T \approx 1$  GK, almost constant during the major part of the shell development (e.g., [41, 42]). In the last day(s) before the SN, temperatures at the base of the C shell may increase due to thermal instabilities in the deeper O-burning layers, and if the C shell is still fully convective, C-shell nucleosynthesis will be revived [42]. At the end of the convective C-burning shell the most abundant isotopes are  $^{16}\text{O}$ ,  $^{20}\text{Ne}$ ,  $^{23}\text{Na}$  and  $^{24}\text{Mg}$ . Sodium is mainly produced via the C-burning reaction  $^{12}\text{C}(^{12}\text{C}, p)^{23}\text{Na}$  and marginally via  $^{22}\text{Ne}(p, \gamma)^{23}\text{Na}$  and  $^{22}\text{Ne}(n, \gamma)^{23}\text{Ne}(\beta^-)^{23}\text{Na}$ . The strongest sodium depletion reaction is  $^{23}\text{Na}(p, \alpha)^{20}\text{Ne}$ , with smaller contributions from  $^{23}\text{Na}(p, \gamma)^{24}\text{Mg}$  and  $^{23}\text{Na}(n, \gamma)^{24}\text{Na}$ .

The impact of the new  $^{23}\text{Na}(n, \gamma)^{24}\text{Na}$  cross section on the weak  $s$ -process distribution was studied with the NuGrid post-processing code MPPNP [43] for a full 25  $M_\odot$  stellar model of solar metallicity [44]. The stellar structure was previously calculated using the GENEC stellar evolution code [45].

By the end of the core He burning phase the  $s$ -process abundance distribution between  $^{56}\text{Fe}$  and  $^{100}\text{Mo}$  was found to be rather insensitive to the MACS values for  $^{23}\text{Na}(n, \gamma)^{24}\text{Na}$ . Although the MACS at 25 keV (25–30 keV is the temperature range of the  $s$  process during core He-burning) is about 10% lower compared to the previous rate [39], the final  $^{23}\text{Na}$  overabundance increases by only a few % and the effect on the  $s$  abundances between Fe and Sr is limited to about 1%. This is explained by the fact that in He core conditions the  $^{23}\text{Na}$  production is marginal, and its abundance coupled with the low MACS implies that the neutron poisoning effect of  $^{23}\text{Na}$  during core He burning is low.

The final  $s$ -abundance distribution at the end of C shell

TABLE VII: Maxwellian averaged cross sections (mb) of the  $^{23}\text{Na}(n,\gamma)^{24}\text{Na}$  reaction

$kT$ (keV)	5	10	15	20	25	30	40	50	60	80	100
This work	$10.1 \pm 0.4$	4.12	2.83	2.30	$2.00 \pm 0.05$	1.80	1.55	1.40	1.30	1.16	1.05
KADoNiS-0.3 <sup>a</sup>	14	5.2	3.4	2.7	2.2	$2.1 \pm 0.2$	1.7	1.5	1.4	1.3	1.2
ENDF/B-VII.1 [30]	13.9	5.24	3.29	2.51	2.09	$1.83 \pm 0.2$	1.52	1.35	1.24	1.09	0.99

<sup>a</sup>Ref. [39]

burning between  $^{56}\text{Fe}$  and  $^{100}\text{Mo}$  obtained with the new  $^{23}\text{Na}(n,\gamma)^{24}\text{Na}$  MACS is compared in Fig. 4 with the distribution based on the previous rate [39]. At this point, the entire isotopic distribution is affected with variations in the order of 5%. At 90 keV thermal energy (typical for the C-burning phase) the new MACS of  $^{23}\text{Na}$  is lower by 13% compared to the previous rate of Bao *et al.* [39]. While the effect on the final overabundance of  $^{23}\text{Na}$  increases only by about 1%, the effect of  $^{23}\text{Na}$  as an important neutron poison in the C shell becomes evident by the propagation effect beyond iron.

Interestingly, the neutron-rich isotopes  $^{70}\text{Zn}$ ,  $^{76}\text{Ge}$ , and  $^{82}\text{Se}$ , which are traditionally considered to be of *r*-only origin, are affected by the new MACS of  $^{23}\text{Na}$  as much as most of the *s*-only isotopes (e.g.,  $^{70}\text{Ge}$  and  $^{76}\text{Se}$ ).

The reduced neutron poison effect of the lower sodium MACS leads to an enhancement of the neutron density, thus increasing the neutron capture probability in the *s*-process branchings. By far the strongest change is obtained for the branching point at  $^{79}\text{Se}$ , where neutron capture on the unstable isotope  $^{79}\text{Se}$  becomes more probable. As a consequence, the  $^{80}\text{Kr}/^{82}\text{Kr}$  ratio is reduced by about 3%. The changes in the  $^{85}\text{Kr}$  branching affect mostly the final abundances of  $^{86}\text{Kr}$  and - by the later decay of  $^{85}\text{Kr}$  - of  $^{85}\text{Rb}$ , rather than those of the related *s*-only isotopes  $^{86,87}\text{Sr}$ . Beyond the abundance peak around Sr, the *s*-process production in massive stars becomes marginal, and the current MACS of  $^{23}\text{Na}$  has a negligible effect.

In the model used in this work the C shell is not convective during the last day before the SN. In models, where the C shell stays convective, the neutron density rises from a few  $10^{11}$  up to a few  $10^{12}$  because all the residual  $^{22}\text{Ne}$  is consumed in  $(\alpha, n)$  reactions at the final increase of the C-burning temperature [42]. In this case, the higher neutron density will lead to a correspondingly larger modification of the abundance pattern in the *s*-process branchings.

It is interesting to note that the higher *s*-process efficiency found with the reduced MACS data for  $^{23}\text{Na}$  is partly compensated by the effect of revised  $(n, \gamma)$  data for the Ne [46] and Mg [47] isotopes. Accordingly, we confirm the conclusion of Heil *et al.* [46] for the weak component, i.e. that "the reproduction of the *s* abundances in the solar system is far from being settled." Accordingly, further improvements of the neutron capture cross sections for heavy species along the *s*-process path and for light neutron poisons are fundamental for constraining *s*-process nucleosynthesis predictions in massive stars.

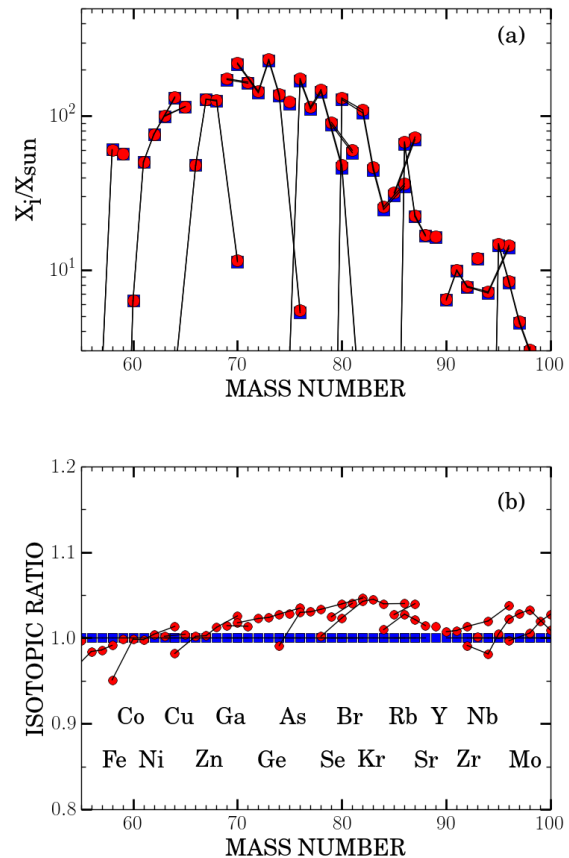


FIG. 4: Color online. Top: Calculated relative *s*-abundance distribution at the end of C shell burning for a  $25 M_{\odot}$  star compared to the distribution obtained with the MACS of  $^{23}\text{Na}$  from the KADoNiS compilation [39]. Bottom: Isotopic ratios emphasizing the reduced neutron poison effect due to the smaller MACS of  $^{23}\text{Na}$  from this work. (Isotopes of the same element are connected by solid lines.)

### C. AGB stars

There are essentially two mechanisms for sodium production in AGB stars. At solar metallicities, sodium is produced primarily during H shell burning where the mixing of protons with the He shell gives rise not only to the formation of a  $^{13}\text{C}$  pocket (where neutrons are produced via the  $^{13}\text{C}(\alpha, n)^{16}\text{O}$  reaction), but also to related  $^{14}\text{N}$  and  $^{23}\text{Na}$  pockets, thus activating the NeNa cycle in

the latter mixing zone [9, 10]. Under these conditions, neutron reactions on sodium are of minor importance.

At low metallicities, however, large amounts of primary  $^{22}\text{Ne}$  are synthesized by conversion of primary  $^{12}\text{C}$  into  $^{14}\text{N}$  during H burning, which is then transformed during He burning by the sequence  $^{14}\text{N}(\alpha, \gamma)^{18}\text{F}(\beta^+ \nu)^{18}\text{O}(\alpha, \gamma)^{22}\text{Ne}$  [9, 48, 49]. This  $^{22}\text{Ne}$  contributes significantly to the primary production of light isotopes, as  $^{23}\text{Na}$  (via  $^{22}\text{Ne}(n, \gamma)^{23}\text{Ne}(\beta^-)^{23}\text{Na}$ ) and  $^{24}\text{Mg}$  (via  $^{23}\text{Na}(n, \gamma)^{24}\text{Na}(\beta^-)^{24}\text{Mg}$ ). Accordingly,  $^{22}\text{Ne}$  and  $^{23}\text{Na}$  are - together with  $^{12}\text{C}$ ,  $^{14}\text{N}$ , and  $^{16}\text{O}$  - major neutron poisons in the  $^{13}\text{C}$  pocket. As shown in the nucleosynthesis studies of Cristallo *et al.* [50] neutron captures on  $^{22}\text{Ne}$  account for about 50% of the total sodium production at very low metallicity ( $Z = 0.0001$ ). For higher metallicities this effect decreases and becomes negligible at  $[\text{Fe}/\text{H}] \geq -1$ .

With the larger neutron exposures in stars of low metallicity, which are characteristic of the strong  $s$ -process component, the highly abundant Ne and Na are either acting as seeds for the reaction flow (enhancing the  $s$ -process production up to Pb/Bi [49]) or as neutron poisons, depending on the efficiency for neutron production in the  $^{13}\text{C}$  pocket.

The effect of the present MACS is illustrated in Fig. 5 for the case of a  $1.5 M_{\odot}$  star with a  $\sim 200$  times lower metallicity compared to solar ( $Z=0.0001$ ). For efficient  $^{13}\text{C}$ -pockets (e.g. for the standard  $^{13}\text{C}$  pocket (ST) adopted in Ref. [2]) the Ne-Na abundances are acting as neutron seeds and are contributing to the  $s$ -process production up to Pb/Bi. With the smaller MACS for  $^{23}\text{Na}$  these contributions are reduced, resulting in the relative reduction of the  $s$ -distribution indicated in the upper panel of Fig. 5. In less efficient  $^{13}\text{C}$  pockets (ST/12) the role of  $^{23}\text{Na}$  as a neutron poison becomes dominant as shown in the lower panel. Due to the smaller MACS, more free neutrons are now available for the  $s$ -process and are leading to an increase of the  $s$ -distribution.

One of the major uncertainties of the  $s$  process in low-mass AGB stars is related to the mixing mechanisms that model the  $^{13}\text{C}$ -pocket. A clear answer to the properties involved in such mixing, possibly resulting from the interplay between different physical processes in stellar interiors (e.g., overshooting, semi-convection, rotation, magnetic fields, see review by Herwig [51] and Refs. [52–54]) has not been reached yet, thus leaving the structure of the  $^{13}\text{C}$ -pocket a persisting problem.

Depending on the shape and extension of the  $^{13}\text{C}$  pocket, the impact of light neutron poisons may affect the  $s$  distribution in different ways. Because the  $^{13}\text{C}$  pocket is artificially introduced in our post-process AGB models, the impact of the new  $^{23}\text{Na}$  MACS could be explored by adopting different shapes and sizes of the  $^{13}\text{C}$  pocket according to recent theoretical and observational indications. From the results obtained in these tests, the  $s$ -distribution was affected by less than  $\sim 5\%$ , independent of the assumptions for the  $^{13}\text{C}$  pocket. Therefore, the improved accuracy of the present MACS provides

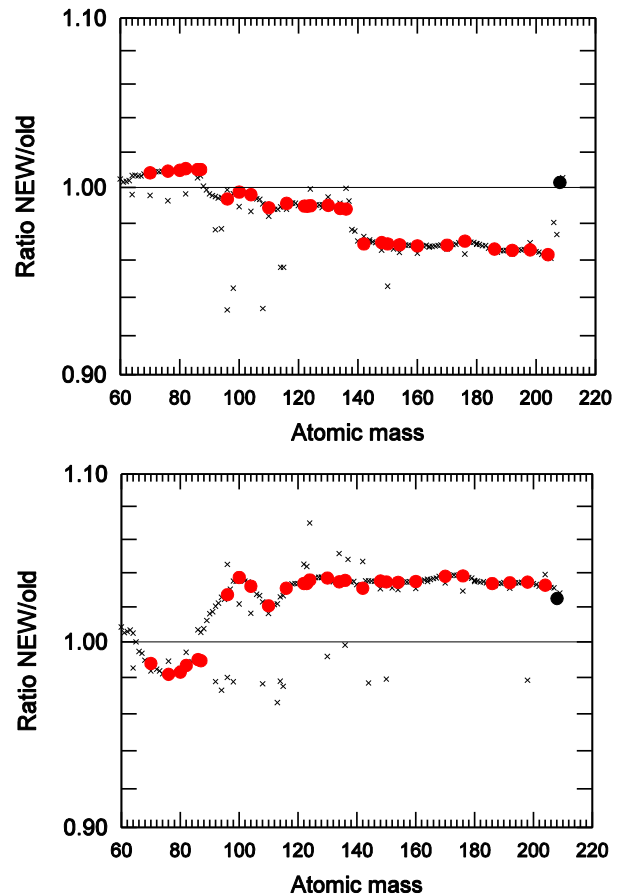


FIG. 5: Color online. The ratio of  $s$ -process yields of a  $1.5 M_{\odot}$  star with  $Z=0.0001$  obtained with the present and old MACS for  $^{23}\text{Na}$ . Pure  $s$ -nuclei are highlighted by full circles, crosses outside the overall distribution are due to branchings in the reaction path. Top: For neutron captures in the  $^{13}\text{C}$  pocket  $^{23}\text{Na}$  acts as an additional seed. This contribution is reduced by the smaller MACS of this work. Bottom: In less efficient  $^{13}\text{C}$  pockets the poisoning effect of  $^{23}\text{Na}$  dominates. Consequently, more free neutrons are available due to the smaller MACS, thus relaxing the poisoning effect.

significant constraints for the neutron poisoning effect of  $^{23}\text{Na}$  in AGB stars.

## V. SUMMARY

The  $^{23}\text{Na}(n, \gamma)^{24}\text{Na}$  cross section has been measured at the Karlsruhe Van de Graaff accelerator in quasi-stellar thermal neutron spectra at  $kT = 5.1$  and  $25$  keV. The resulting Maxwellian averaged cross sections of  $\langle \sigma \rangle_{kT=5\text{keV}} = 9.1 \pm 0.3$  mb and  $\langle \sigma \rangle_{kT=25\text{keV}} = 2.03 \pm 0.05$  mb are significantly smaller compared to the recommended values of the KADoNiS-v0.3 compilation [39]. After reducing the radiative width of the prominent s-wave resonance at  $2.8$  keV by  $35\%$ , the measured cross sections were found perfectly compatible with the set of



resonance data in the ENDF/B-II.1 library.

With this modification, Maxwellian averaged cross sections in the relevant range of thermal energies between  $kT = 5 - 100$  keV were derived using the energy dependence obtained by an R-matrix calculation with the SAMMY code [32]. The effect of the present cross section on the  $s$  process abundances in massive stars (weak  $s$  process) is quite small during the He core burning phase, but becomes significant during the carbon-shell burning phase where  $^{23}\text{Na}$  is synthesized in increasing quantities via the  $^{12}\text{C}(^{12}\text{C}, p)^{23}\text{Na}$  reaction. The impact of the present MACS measurement has been investigated within a massive star model. It was found that the new lower MACS causes a propagation effect over the entire weak  $s$ -process distribution, with a general abundance increase of about 5%.

### Acknowledgements

The authors are thankful to D. Roller, E.-P. Knaetsch, W. Seith, and the entire Van de Graaff group for their support during the measurements. EU would also like to acknowledge the support of JINA (Joint Institute

for Nuclear Astrophysics), University of Notre Dame, Notre Dame, IN, USA. SB acknowledges financial support from JINA (Joint Institute for Nuclear Astrophysics, University of Notre Dame, IN) and KIT (Karlsruhe Institute of Technology, Karlsruhe, Germany). MP acknowledges support from NuGrid by NSF grant PHY 09-22648 (Joint Institute for Nuclear Astrophysics, JINA), NSF grant PHY-1430152 (JINA Center for the Evolution of the Elements), and EU MIRG-CT-2006-046520. He also appreciates support from the "Lendulet-2014" Programme of the Hungarian Academy of Sciences (Hungary) and from SNF (Switzerland). MP also acknowledges PRACE, through its Distributed Extreme Computing Initiative, for resource allocations on Sisu (CSC, Finland), Archer (EPCC, UK), and Beskow (KTH, Sweden) and the support of STFCs DiRAC High Performance Computing Facilities; DiRAC is part of the National E-infrastructure. Ongoing resource allocations on the University of Hulls High Performance Computing Facility - viper - are gratefully acknowledged. CL acknowledges support from the Science and Technology Facilities Council UK (ST/M006085/1).

- 
- [1] C. Raiteri, R. Gallino, M. Busso, *et al.*, *Ap. J.* **419**, 207 (1993).
- [2] R. Gallino, C. Arlandini, M. Busso, *et al.*, *Ap. J.* **497**, 388 (1998).
- [3] F. Käppeler, R. Gallino, S. Bisterzo, and W. Aoki, *Rev. Mod. Phys.* **83**, 157 (2011).
- [4] F.-K. Thielemann W.D. and Arnett, *Ap. J.* **295**, 604 (1985).
- [5] S. Woosley, A. Heger, and T. Weaver, *Rev. Mod. Phys.* **74**, 1015 (2002).
- [6] C. Kobayashi, H. Umeda, K. Nomoto, *et al.*, *Ap. J.* **653**, 1145 (2006).
- [7] S. Lucatello, T. Masseron, J.A. Johnson, *et al.*, *Ap. J.* **729**, 40L (2011).
- [8] C. Raiteri, M. Busso, R. Gallino, *et al.*, *Ap. J.* **367**, 228 (1991).
- [9] N. Mowlavi, *Astron. Astrophys.* **350**, 73 (1999).
- [10] S. Goriely and N. Mowlavi, *Astron. Astrophys.* **362**, 599 (2000).
- [11] S. Cristallo, L. Piersanti, O. Straniero, *et al.*, *The Astrophysical Journal Supplement* **197**, (2011), <http://adsabs.harvard.edu/abs/2011ApJS..197...17C>.
- [12] A. Karakas, *Mon. Not. Royal Astron. Soc.* **403**, 1413 (2010).
- [13] M. Busso, R. Gallino, and G. Wasserburg, *Ann. Rev. Astron. Astrophys.* **37**, 239 (1999).
- [14] S. Cristallo, R. Gallino, O. Straniero, *et al.*, *Mem. Soc. Astron. Italiana* **77**, 774 (2006).
- [15] S. Bisterzo, R. Gallino, O. Straniero, S. Cristallo, and F. Käppeler, *MNRAS*, 404, 1529 (2010).
- [16] P. Ventura and F. D'Antona, *Mon. Not. R. Astron. Soc.* **410**, 2760 (2011).
- [17] S. Straniero, S. Cristallo, and L. Piersanti, *Ap. J.* **785**, 77 (2014).
- [18] A. de L. Musgrove, B. Allen, and R. Macklin, in *Neutron Physics and Nuclear Data for Reactors and other Applied Purposes* (OECD, Paris, 1978), p. 426.
- [19] P. Koehler, R.R. Winters, K.H. Guber, *et al.*, *Phys. Rev. C* **62**, 055803 (2000).
- [20] H. Beer and F. Käppeler, *Phys. Rev. C* **21**, 534 (1980).
- [21] W. Ratynski and F. Käppeler, *Phys. Rev. C* **37**, 595 (1988).
- [22] C. Lederer, F. Käppeler, M. Mosconi, *et al.*, *Phys. Rev. C* **85**, 055809 (2012).
- [23] G. Feinberg, M. Friedman, A. Krasa, *et al.*, *Phys. Rev. C* **85**, 055810 (2012).
- [24] M. Heil, S. Dababneh, A. Juseviciute, *et al.*, *Phys. Rev. C* **71**, 025803 (2005).
- [25] S. Dababneh, N. Patronis, P.A. Assimakopoulos, *et al.*, *Nucl. Instr. Meth.* **A517**, 230 (2004).
- [26] S. Agostinelli, J. Allison, K. Amako, *et al.*, *Nucl. Instr. Meth. A* **506**, 250 (2003).
- [27] P. Endt, J. Blachot, R. Firestone, and J. Zipkin, *Nucl. Phys. A* **633**, 1 (1998).
- [28] Z. Chunmei, *Nucl. Data Sheets* **95**, 59 (2002).
- [29] JEFF report 21 (OECD Nuclear Energy Agency, Paris, 2006), <https://www.oecd-nea.org/dbdata/jeff/>.
- [30] I. Dillmann, R. Plag, F. Käppeler *et al.*, in *Nuclei in the Cosmos XIII*, edited by Z. Fülöp (SISSA, Trieste, 2014), POS (NIC-XIII) 57, <http://pos.sissa.it>.
- [31] Z.Y. Bao, H. Beer, F. Käppeler, *et al.*, *Atomic Data Nucl. Data Tables* **76**, 70 (2000).
- [32] N. Larson, Report ORNL/TM-9179/R7, (Oak Ridge National Laboratory, Oak Ridge, 2006).
- [33] M. Chadwick *et al.*, *Nuclear Data Sheets* **112**, 2887 (2011).

- [34] A. Mengoni, T. Otsuka, and M. Ishihara, *Phys. Rev. C* **52**, R2334 (1995).
- [35] J. Tomandl, J. Novák, V. Burjan, *et al.*, *Phys. Rev. C* **69**, 014312 (2004).
- [36] R. Firestone, Z. Revay, and T. Belgya, *Phys. Rev. C* **89**, 014617 (2014).
- [37] S. Mughabghab, in *Atlas of Neutron Resonances, 5<sup>th</sup> Edition* (Elsevier, Amsterdam, 2006).
- [38] A. Friesenhahn, W. Lopez, F. Froehner, *et al.*, in *Neutron Cross sections and Technology*, Vol. II of *NBS Special Publications 299* (Natl. Bureau of Standards, Washington D.C., 1968), p. 695.
- [39] I. Dillmann, R. Plag, F. Käppeler, and T. Rauscher, in *EFNUDAT Fast Neutrons - scientific workshop on neutron measurements, theory & applications*, edited by F.-J. Hamsch (JRC-IRMM, Geel, 2009), pp. 55 – 58, <http://www.kadonis.org>.
- [40] T. Rauscher, P. Mohr, I. Dillmann, and R. Plag, *Ap. J.* **738**, 143 (2011).
- [41] L. The, M. El Eid, and B. Meyer, *Ap. J.* **655**, 1058 (2007).
- [42] M. Pignatari, R. Gallino, M. Heil, *et al.*, *Ap. J.* **710**, 1557 (2010).
- [43] F. Herwig, S. Diehl, C.L. Fryer, *et al.*, in *Nuclei in the Cosmos X*, edited by H. Schatz *et al.*, (SISSA, Trieste, 2008), PoS (NIC-X) 23, <http://pos.sissa.it>.
- [44] M. Pignatari, R. Hirschi, M. Wiescher, *et al.*, *Ap. J.*, **762**, 31 (2013).
- [45] P. Eggenberger, G. Meynet, A. Maeder, *et al.*, *Astrophys. Space Sci.* **316**, 43 (2008).
- [46] M. Heil *et al.*, *Phys. Rev. C* **90**, 045804 (2014).
- [47] C. Massimi, P. Koehler, S. Bisterzo, and the n\_TOF collaboration, *Phys. Rev. C* **85**, 044615 (2012).
- [48] R. Gallino, S. Bisterzo, L. Husti, *et al.*, in *Nuclei in the Cosmos IX*, edited by A. Mengoni *et al.*, (SISSA, Trieste, 2007), PoS (NIC-IX) 100, <http://pos.sissa.it>.
- [49] L. Husti, R. Gallino, S. Bisterzo, *et al.*, *Mem. Soc. Astron. It.* **78**, 523 (2007).
- [50] S. Cristallo, O. Straniero, R. Gallino, *et al.*, *Ap. J.* **696**, 797 (2009).
- [51] F. Herwig, *Ann. Rev. Astron. Astrophys.* **43**, 435 (2005).
- [52] O. Straniero, R. Gallino, and S. Cristallo, *Nucl. Phys. A*, **777**, 311 (2006).
- [53] A.I. Karakas and J.C. Lattanzio, *Pub. Astronom. Soc. Australia*, **31**, e030 (2014).
- [54] M.C. Nucci and M. Busso, *Ap. J.* **787**, 141 (2014).